The International Journal of Advanced Manufacturing Technology (2019) 101:1495–1508
https://doi.org/10.1007/s00170-018-3000-z

ORIGINAL ARTICLE

An efficient coupled Eulerian-Lagrangian finite element model for friction stir processing

Mohammad Ali Ansari[1] · Avik Samanta[2] · Reza Abdi Behnagh[3] · Hongtao Ding[2]

Received: 6 June 2018 / Accepted: 5 November 2018 / Published online: 21 November 2018

Abstract
Friction stir processing (FSP) is a friction stir-based material processing method for enhancement of material microstructural and surface properties. As FSP is a multi-physics problem coupled with severe plastic deformation, material flow, heat flow, and microstructure evolution, modeling of the FSP process can be very complicated and challenging. Few research work has been reported on modeling and simulations of FSP for material modification. In this study, a computation-efficient process model is developed using ABAQUS/Explicit based on coupled Eulerian-Lagrangian (CEL) formulation to simulate FSP of aluminum alloy 5083. The three-dimensional (3D) finite element model simulates the entire process of FSP including tool plunging, dwelling, and stirring phases. Simulations are performed to evaluate the effects of tool-rotational speed and tool pin profile during the FSP process. The computational efficiency of the developed model is also evaluated in comparison with other existing models for friction stir–welding processes. FSP experiment is performed with measurements of process force and temperature for model validation. This study shows that the CEL model can be a powerful numerical tool to simulate the complex process mechanics and optimize the FSP process parameters for industrial applications.

Keywords Friction stir processing · Coupled Eulerian-Lagrangian · Finite element model · Aluminum alloy

1 Introduction

Friction stir processing (FSP) is a mechanical deformation-based, solid-phase process to modify the material surface and microstructure properties utilizing a similar friction stir principle as friction stir welding (FSW) [1–3]. Characteristically different from the FSW process though, FSP is not to join materials but mainly used to change metal part surface microstructure and mechanical properties. During the FSP process, a nonconsumable tool with complex features is applied at a high rotational speed to modify work material. The workpiece material does not reach the melting temperature, but typically reaches a malleable or softened state that promotes the stirring and mixing of the workpiece material. The FSP process consists of three stages: plunging, dwelling, and stirring [4, 5], as illustrated in Fig. 1. The process starts by inserting the rotational tool into the workpiece until the tool shoulder touches the work material surface and the target depth is reached. Then, during the dwelling stage, the tool is kept for a few seconds at the desired depth in the work plate, while the frictional heat generated at the tool-work material interface softens the work material significantly. During the stirring step, the tool stirs the work material along the designated path at a controlled rotational and translational speed [6–9], while the work material is stirred from the front end of the tool to the back end resulting in a solid-state mixing. By carefully designing the tool and selecting the process conditions [2, 10, 11], this process has been successfully applied to enhance the target material performances including refinement of microstructure [1, 12, 13], homogenization and

✉ Hongtao Ding
hongtao-ding@uiowa.edu

Mohammad Ali Ansari
mansari3@wisc.edu

Avik Samanta
avik-samanta@uiowa.edu

Reza Abdi Behnagh
r.abdibehnagh@mee.uut.ac.ir

[1] Department of Mechanical Engineering, University of Wisconsin-Madison, Madison, USA

[2] Department of Mechanical and Industrial Engineering, University of Iowa, Iowa City, IA 52242, USA

[3] Faculty of Mechanical Engineering, Urmia University of Technology, Urmia, Iran

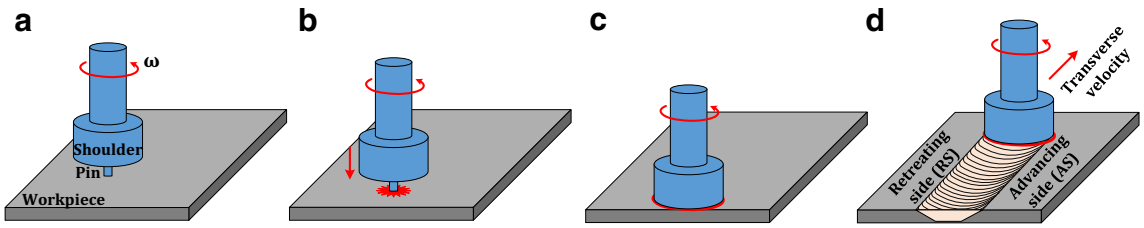

Fig. 1 Schematic of the FSP process steps: **a** nonconsumable tool with complex features rotates; **b** the rotational tool is plunged into the workpiece until the tool shoulder touches the work material; **c** the tool dwells at the desired depth to generate enough frictional heat to soften the material; **d** the tool is moved along the surface with controlled rotational and translational speed

elimination of porosity [14, 15], and increase of corrosion resistance [16, 17].

Fundamental understanding of the process principles is critically needed for the design, optimization, and industrial application of the FSP process. As FSP is a multi-physics problem coupled with severe plastic deformation, material flow, heat flow, and microstructure evolution, modeling of the FSP process can be very complicated and challenging. The variation of the material flow velocity around the tool peripheral due to the effect of translational and rotational speed leads to a nonsymmetric condition in terms of heat, stress, and plastic deformation at the advancing and retreating sides of the workpiece. The amount of heat and plastic deformation around the stirred zone further influences the final material microstructure and mechanical properties. The resultant workpiece domain typically consists of three distinct microstructural zones, i.e., stirred zone (SZ), thermomechanically affected zone (TMAZ), and heat-affected zone (HAZ) [18]. Dynamic recrystallization (DRX) is often induced within SZ and results in a fine recrystallized grain structure of the area [19–24]. A homogenized microstructure with equiaxed fine grains in this area leads to improvements in mechanical properties such as ductility, formability, and mechanical properties [25, 26]. The shape and size of SZ are mostly dependent on the process parameters applied, such as the tool-rotational speed, traverse speed, tool shape, and tool size. Next to SZ, there exists TMAZ with typically elongated grain structures. The third region outside TMAZ is HAZ, which is thermally affected by the process while without obvious plastic deformation. The tool design also plays a crucial part in the creation of the final product affecting the material flow, heat generation, final microstructure, and properties of the processed surface. Geometrical features of the tool in terms of pin height and shape, shoulder surface pattern, and diameter needs to be well designed to achieve desirable surface properties [27].

Most of the existing FSP research relies on experimental methods. Indeed, extensive experimental studies have been carried out for various engineering alloys such as aluminum [14, 15], steel [16, 28], magnesium [17, 29], and titanium alloys [30]. However, few research work has been reported on modeling and simulations of FSP for material modification. This work is aimed at the development of a computation-efficient process model for the FSP process as it can be applied as a useful numerical tool to minimize the number of experimental studies, increase the procedure efficiency in terms of time and cost, and contribute to a better fundamental comprehension of the process mechanics and improved knowledge-driven manufacturing process planning.

The existing modeling work in literature was mostly developed for the FSW process for joining materials [31–40]. In the non-flow-based models, simulation abortion often happens due to the excessive mesh distortion of Lagrangian domains. Arbitrary Lagrangian-Eulerian (ALE) technique and adaptive remeshing are usually used to avert excessive mesh distortion [37–40]. The ALE formulation is used to preserve a good mesh quality throughout the computation of the FSW process [41, 42]. However, severe mesh distortion due to the stirring effect of the FSW process led to premature failure of the simulation with ALE formulation. Chiumenti et al. [43] developed a sliding mesh around the tool pin that rotates together with the pin (ALE formulation), to avert the severe distortion of the mesh in the stirring zone. The rest of the mesh was kept as Eulerian formulation. The flow of the material was visualized by particle tracing [44]. However, this technique could not completely eliminate the mesh distortion and it is also computationally expensive.

Recently, coupled Eulerian-Lagrangian (CEL) models have been developed to simulate severe plastic deformation in the FSW process [31–36, 45–48]. In this method, the workpiece domain is modeled through Eulerian formulation, so that potential excessive mesh distortion can be avoided during the simulation. Initially, CEL model was used for predicting thermomechanical response in terms of force signal and temperature profile [31–33, 35]. Later, researchers used CEL model to study the material flow during FSW [46, 48, 49]. Marker material technique was used in the CEL model to study the material flow mechanism. Most of the vertical material flow is observed on the advancing side in comparison with the retreating side [49]. In addition, insufficient material flow led to a hook defect in the FSW process in AA6061 alloy [48]. Some studies used CEL methods to predict defects during the FSW process [34, 36, 45, 46]. Ajri and Shin [36] developed CEL-based process models in ABAQUS/Explicit to predict likely conditions that result in defect generation including tunnel defects, cavities, and excess flash formation

during the FSW process. Tunnel defects have been successfully predicted using CEL methods for different welding parameters [45]. Their modeling work shows that pin height and tool tilt angle play an important role in eliminating tunnel defect. The effect of material flow and thermal cycle on hook defect in the joint interface was also studied during the FSW process using CEL method [46]. In recent years, coupled Eulerian-Lagrangian (CEL) models have been developed to simulate severe plastic deformation processes, such as rolling [50], machining [51, 52], and friction stir extrusion [53]. There was no mesh distortion in CEL modeling that significantly improve the modeling of severe deformation processes. ALE and CEL methods were compared for modeling orthogonal cutting [54], and CEL model was found to be the most computationally efficient modeling technique for severe plastic deformation process. Unlike ALE, CEL technique can handle severe distortion of the mesh without premature failure of the simulation. However, one key remaining issue is the computational cost associated with the CEL modeling of complex friction stir processes [7, 34, 55].

In summary, the modeling of FSP comprises significant challenges as it is a complicated multi-physics problem with severe plastic deformation at elevated temperature, complicated material flow around the tool, tool material interaction, near liquid-soft state of work material, and material property change due to microstructure evolution during the process. It is important to decouple those complicated physics problems to ease out computational effort. In the current study, a computation-efficient CEL model is developed using ABAQUS/Explicit to simulate the thermomechanical aspect of the complete FSP process including plunging, dwelling, and stirring phases for aluminum alloy 5083. A mass scaling technique was employed in the developed CEL model to improve computational efficiency. FSP experiments are also performed to collect data of temperatures and forces for model validation to show that implementing mass scaling does not compromise the simulated results. Most of the reported FSP work only evaluated the cylindrical tool profile. In this work, the effects of FSP process parameters and various tool designs are evaluated for the process outputs such as force, temperature, and strain rate using the CEL model. The main objective of this work is to present an efficient CEL model for the FSW process and validate the model with experimental results to show that the techniques applied to make the model do not compromise the model prediction. The model is further applied for different tool pin design to provide a guideline for the efficient tool design.

2 Experiments

In this study, a vertical CNC milling machine was retrofitted to perform FSP experiments. The work material was AA5083-H111 plates with a dimension of $100 \times 150 \times 5$ mm^3. The chemical composition of this alloy is shown in Table 1. Table 2 lists all the experimental parameters for this study. Most of the experiments used a cuboid tool with a dimension of $3 \times 3.5 \times 3.5$ mm^3 and shoulder diameter of 18 mm. The FSP tools were made of AISI D6 tool steel. The FSP process started by inserting the rotational tool into the plate with the speed of 45 mm/min until the tool shoulder touched the plate surface. The rotating tool was kept at the desired depth for 2 s to increase the temperature. Finally, the tool was moved with a constant traverse speed of 50 mm/min while rotated in a clockwise direction. In all cases, the initial temperature of the tool and workpiece was 25 °C. Each experimental condition was repeated three times to assure the repeatability. During the experiments, a three-axis dynamometer and multiple K-type thermocouples were applied for measuring forces and temperatures, respectively. The thermocouples were embedded into the sheet at locations of 4, 8, 12, and 16 mm away from the center line in both advancing and retreating sides (as illustrated in Fig. 2).

Figure 3 shows the top view of the friction stir processed AA5083 with 1000 rpm rotational speed and 50 mm/min traverse speed. The top surface is without crack or any visible defects. The surface also exhibits very smooth quality with stirring rings.

After the experiments, the processed plate was sectioned perpendicular to the feed direction to investigate the stirred zone area. The samples were polished and etched for metallography analysis using modified Poulton's reagent for 1 min to reveal the grain boundaries. The reagent contained 12 mL HCl (concentrated), 16 mL HNO_3 (concentrated), 1 mL H_2O, and 1 mL HF (48%), and 16 mL of diluted chromic acid which contained 3 g of chromic acid per 10 mL H_2O.

3 Modeling

3.1 Coupled Eulerian-Lagrangian finite element model

A three-dimensional CEL model was developed in this work and solved using ABAQUS/Explicit to simulate the plunging, dwelling, and stirring phases during the FSP process. In the model, the workpiece was considered as a Eulerian domain whereas the FSP tool was modeled using Lagrangian formulation. Due to the localized deformation during the FSP process and low-computational efficiency, the Eulerian domain size was considered according to the stress-free inflow condition. The selection of domain size was a trade-off between accuracy and computational cost. A size equivalent to four times of the tool shoulder diameter was chosen for optimizing both of them [34, 56, 57]. The Eulerian part thickness was kept

Table 1 The chemical composition of the AA5083-H111 (wt.%)

Al	Si	Fe	Cu	Mn	Mg	Cr	Zn	Ti
Balance	0.1	0.31	0.04	0.61	4.27	0.1	0.02	0.026

as 5 mm, equal to the thickness of the work material plate during the experiment. The Eulerian domain was generated in a cuboid shape, having a volume of 72 × 72 × 5 mm^3 (Fig. 4). Due to the accuracy improvement and program time reduction, the biased-meshing technique was applied to generate a fine mesh for the interaction of the workpiece and rigid FSP tool and coarse mesh in the sides. The Eulerian workpiece body was meshed through 30,444 thermally coupled Eulerian elements (EC3D8RT), having 4° of freedom for nodes (the numerical mesh is presented in (Fig. 5a). The stirring phase of the process was simulated by defining the traverse speed as an inflow and outflow for the Eulerian domain (Fig. 4) [34]. It is important to note that in the CEL formulation, there is no mesh movement in the Eulerian domain and the material flows through the mesh.

The tool was modeled as an isothermal Lagrangian rigid body formulation in which thermally coupled 4-node 3D bilinear rigid quadrilateral element was used to generate the mesh (Fig. 5b). All of the movement conditions were assigned with respect to the tool reference point to control the tool motion accurately. The tool had two different speeds during the simulation. Firstly, it was constrained in the target depth with a rotational speed around its local axis, and then the workpiece material flowed into the Eulerian mesh with the inflow and outflow velocity, i.e., equal to negative traverse speed. During the plunging stage, there is no inflow, and outflow velocity input condition is applied. Only the tool-rotational speed is applied. On the other hand, both rotational speed, inflow and outflow velocity is applied during the stirring phase. In addition, velocity constraints were applied at the bottom and sides of the workpiece to avoid the material movement from the domain boundaries. The modeling conditions were defined according to FSP experimental process parameters in terms of plunging speed, rotational speed, dwelling time, stirring speed, tool tilt angle, and plunge depth. A heat sink was applied at the bottom side of the workpiece to accommodate the heat dissipation into the surroundings.

Table 2 Process parameters employed in this study

Test	Rotational speed (rpm)	Plunging speed (mm/min)	Traverse speed (mm/min)
1	600	45	50
2	800		
3	1000		
4	1200		

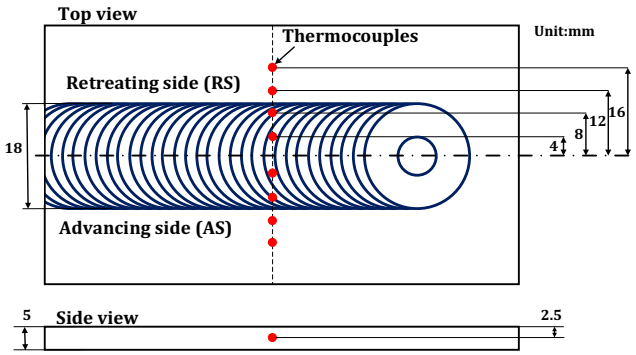

Fig. 2 Thermocouples location in the workpiece

3.2 Model formulations

In the CEL model developed in this study, the workpiece domain was modeled using Eulerian formulation where mass, momentum, and energy are conserved, as shown in Eqs. 1–3 [58]. The mass conservation equation takes care of the rate at which the mass changes inside the control volume and the mass outflow rate. The momentum conservation equation equals the change of momentum of the domain to the sum of the spatial time derivative of the Cauchy stress tensor and the gravitational force. The energy equation incorporates the rate of work done on any element, the heat flux into the element due to conduction, and the volumetric heat generation from the element.

$$\frac{\partial \rho}{\partial t} + \nabla.(\rho \mathbf{v}) = 0 \tag{1}$$

$$\rho\left(\frac{\partial \mathbf{v}}{\partial t} + \nabla.(\mathbf{v}\otimes\mathbf{v})\right) = \nabla.\boldsymbol{\sigma} + \rho\mathbf{g} \tag{2}$$

$$\rho C_p\left(\frac{\partial T}{\partial t} + \mathbf{v}.\nabla T\right) = \nabla.(K\nabla T) + \nabla.(\boldsymbol{\sigma}.\mathbf{v}) + \dot{Q} \tag{3}$$

where ρ is the material density; σ is the Cauchy stress tensor; g is the gravitational constant; C_p is the specific heat; K is the thermal conductivity of the material; T is the temperature in Kelvin scale; and $\dot{Q}$ represents the volumetric heat generation rate.

The governing equations are split into Lagrangian step and Eulerian step through the employment of operator splitting algorithm [58, 59]. After splitting, the corresponding equations for the Lagrangian step and Eulerian steps are formed as Eq. 4 and Eq. 5 respectively [59]:

$$\frac{\partial \varphi}{\partial t} = S \tag{4}$$

$$\frac{\partial \varphi}{\partial t} + \nabla.\Phi = 0 \tag{5}$$

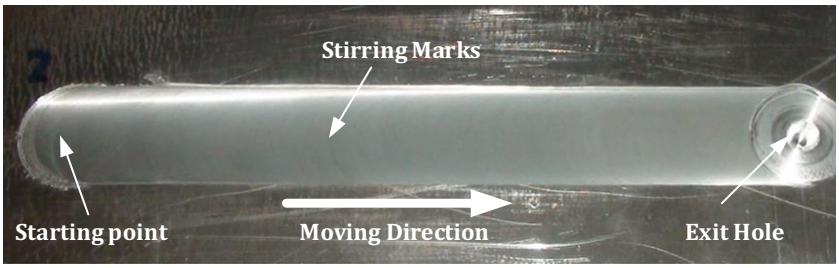

Fig. 3 Top surface of the FSP specimen

where Φ and S are the flux function and source term, respectively. The flux function term Φ in the Eulerian step corresponds to the second term on the left-hand side of each equation. The source term S in Lagrangian step corresponds to the terms on the right side of each equation. The numerical calculation in the Lagrangian step governs the change of mass, momentum, and energy based on the applied forces. The deformed mesh from the Lagrangian step will be restored to its original shape in the Eulerian step. The mass, momentum, and energy are modified between adjacent elements using transport algorithms.

Because FSP is a coupled thermomechanical problem, in this work, the process is modeled assuming heat generation via inelastic work in sticking condition and ignoring the frictional heat during slipping. Thus, the temperature distribution is solved by considering heat generation governed by Fourier law related to heat conduction [60]:

$$K\nabla^2 T + \dot{Q} = \rho C_p \frac{\delta T}{\delta t} \tag{6}$$

It should be noted that ρ, K, and C_p are temperature dependent, and heat generation rate is [61]:

$$\dot{Q} = \dot{Q}_f + \dot{Q}_p \tag{7}$$

where, $\dot{Q}_f$ is the heat generation rate due to friction and $\dot{Q}_p$ is the heat generation rate due to plastic deformation which is given by:

$$\dot{Q}_p = \propto (\boldsymbol{\tau} \times \dot{\varepsilon}) \tag{8}$$

where $\propto$ is conversion factor which is assumed to 1 in this study, $\boldsymbol{\tau}$ is shear stress, and $\dot{\varepsilon}$ is plastic strain rate tensor.

Furthermore, during the FSP process, the workpiece is clamped on the table, and the tool applies the pressure on the workpiece surface. Due to the lack of pressure, positive stress exists on the workpiece top, and smaller negative stress is revealed in between of workpiece and backing plate [62]. This phenomenon results in a large thermal resistance in the interface of the workpiece and backing plate which is based on the interstitial gaseous medium gap between two plates [63]. Due to the complicated condition of heat transfer between the backing plate and workpiece, the problem is simplified by considering only the convection heat transfer which shows a good agreement between experimental and simulation output in different studies [64–66]. Hence, in this study, the same condition is applied.

In addition, the FSP process has heat dissipation from the workpiece surfaces to the air through radiation and convection:

$$-\mathrm{K}\frac{\partial T}{\partial \delta_s} = \varphi_b \epsilon_b \left(T^4 - {T_a}^4\right) + \gamma_{con}(T - T_a) \tag{9}$$

where δ_s is the normal direction to the surface of heat dissipation, ϵ_b is the emissivity, φ_b is the Stefan-Boltzmann constant, T_a is the peripheral temperature, and γ_{con} is the convective heat transfer coefficient. In the current study, the ϵ_b, γ_{con}, and the peripheral temperature is set to 0.09, 10 W/m^2 °C, and 25 °C, respectively [35, 67].

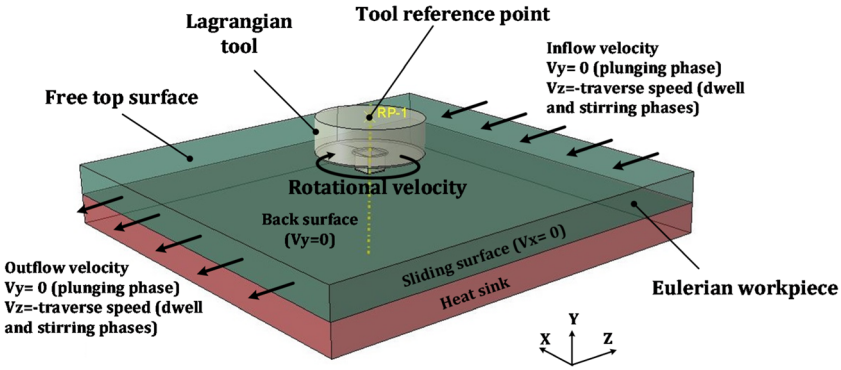

Fig. 4 CEL model boundary conditions

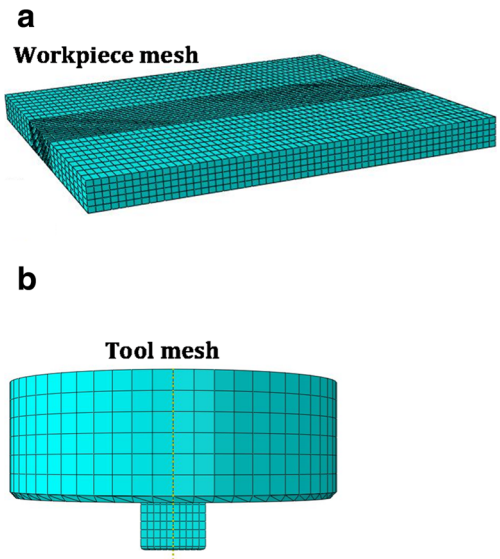

Fig. 5 Mesh of the CEL model: **a** Eulerian mesh of the workpiece and **b** Lagrangian mesh of the tool

3.3 Mass scaling

To minimize the simulation time, mass scaling technique was employed in this simulation. Mass scaling technique has been used to improve the simulation efficiency of CEL formulation during simulation of forming process [68]. In this technique, the thermal properties are adapted to keep thermal time steady. Thus, it can be employed even with rate-dependent or time-dependent parameters. To formulate the thermo-elasticity of material, the Navier's equation is employed [69]:

$$\mu\nabla^2\mathbf{u} + (\lambda+\mu)\nabla tr(\mathbf{E}) - \alpha\lambda\nabla T = \rho\frac{\delta^2 u}{\delta t^2} \tag{10}$$

where $\boldsymbol{u}$, $\boldsymbol{E}$, α, and ρ are displacement vector, linear strain tensor, thermal expansion coefficient, and density, respectively; λ and μ are Lamé coefficients.

Replacing the density by fictitious density $\rho^* = k_m\rho$ ($k_m > 1$), Eq. 10 is scaled in terms of mass. The value of k_m was chosen by considering the inertial forces in the right-hand side of Eq. 10. By exchanging the density by fictitious density, the scaled thermoelastic equation is as follows:

$$\mu\nabla^2\mathbf{u} + (\lambda+\mu)\nabla tr(\mathbf{E}) - \alpha\lambda\nabla T = \rho^*\frac{\delta^2 u}{\delta t^2} \tag{11}$$

Therefore, the substantial increase in the right-hand side of Eq. 11 results in a small steady time increment of the explicit solver which decreases the simulation time. To achieve a reasonable accuracy of the simulation results accuracy, the ratio of kinetic energy to internal energy should be less than 1% which is checked for the simulated model.

3.4 Material modeling

The constitutive material model of AA 5083 was expressed by Johnson-Cook's [70] model:

$$\sigma = \left(A + B\bar{\varepsilon}_{\mathrm{pl}}^{\,n}\right)\left(1 + C\ln\frac{\dot{\bar{\varepsilon}}_{\mathrm{pl}}}{\dot{\varepsilon}_0}\right)\left(1-\left(\frac{T-T_{\mathrm{ref}}}{T_{\mathrm{melt}}-T_{\mathrm{ref}}}\right)^m\right) \tag{12}$$

where $\bar{\varepsilon}_{\mathrm{pl}}$, $\dot{\bar{\varepsilon}}_{\mathrm{pl}}$, and $\dot{\varepsilon}_0$ are the effective plastic strain, the effective plastic strain rate, and the normalized strain rate, respectively. A, B, C, n, and m are material constants, which consider the effects of strain hardening, thermal softening, and strain rate sensitivity, respectively. In addition, T_{ref} and T_{melt} represent the ambient temperature and the material solidus temperature, respectively. Tables 3 and 4 represent the Johnson-Cook parameters and thermal and elastic properties of AA 5083 [35, 71, 72], respectively. Those properties were considered as temperature dependent in this simulation.

3.5 Friction model at the tool-workpiece interface

The critical part of FSP simulation is modeling the contact condition between the tool and workpiece as the Eulerian workpiece domain interacts with the Lagrangian tool domain. The Coulomb coefficient is defined as a term of contact pressure, slip rate, and average surface temperature at the contact point [73]. Various studies investigated contact models for the friction stir–welding process, and most of them applied constant friction coefficient during the simulation to match with the process output fields [55]. Due to the formation of the large volume of plasticized material during the FSP process, visco-plastic friction dominates the friction performance and heat generation depends on excessive plastic deformation at the interface of the tool and the workpiece. Therefore, in this study for FSP, the most suitable friction law is the modified Coulomb friction law [57, 74] in which the contacting interface shear stress is defined as [75]:

$$\tau_{\mathrm{friction}} = \tau_{\mathrm{shear}} = \begin{cases} \mu_f p, \text{for } \mu_f p < \tau_{\max} \\ \dfrac{\sigma_s}{\sqrt{3}}, \text{for } \mu_f p > \tau_{\max} \end{cases} \tag{13}$$

Table 3 Johnson-Cook plasticity model constant for AA 5083 [35]

Material	A [MPa]	B [MPa]	C	n	m	T_{ref} [°C]	T_{melt} [°C]
AA 5083	170	425	0.0335	0.42	1.225	25	640

Table 4 Temperature-dependent physical properties of AA 5083 [71, 72]

Temp. (°C)	Conductivity (W/m °C)	Specific heat (J/ kg °C)	Density (kg/m^3)	Temp. (°C)	Thermal expansion (10^{-6}/°C)	Temp. (°C)	Young's modulus (GPa)
25.0	112.5	924.1	2673.9	25	23.8	25	70 .0
80.0	122.7	984.2	2642.7	200	25.5	100	67.8
180.0	131.6	1039.6	2629.4	300	26.8	200	60.7
280.0	142.3	1081.2	2611.5	400	28.9	300	51.0
380.0	152.5	1136.6	2589.3	500	31.5	400	37.4
480.0	159.5	1178.2	2567.0	–	–	–	–
580.0	177.2	1261.4	2549.2	–	–	–	–

where τ_{friction}, τ_{shear}, μ_f, p, and σ_s are the friction shear stress, flow shear stress, friction coefficient, contact pressure, and equivalent flow stress respectively.

4 Results and discussions

4.1 Determination of friction coefficient and model validation

To determine the coefficient of friction, six CEL simulations were performed with various values of coefficient of friction. The rotational speed and traverse speed was kept constant at 1000 rpm, and 50 mm/min respectively. The experimental and simulated results were compared in terms of temperature distribution 4 mm away from the stirring zone center line, 5 s after the beginning of stirring phase. In addition, forces in the axial and transverse directions and micrograph of the cross-section were also compared to find out the suitable coefficient of friction. The maximum temperature was extracted at a 4-mm distance from the center line of the stirred zone for all six simulation conditions and plotted in Fig. 6a. As the coefficient of friction value increases the temperature increases in a linear fashion. Similarly, mean forces in axial and transverse direction were extracted from the simulation output file and plotted in Fig. 6b and Fig. 6c respectively. As the coefficient of friction increases, both the forces decrease exponentially.

The mean absolute percentage error (MAPE) (Eq. 14) for maximum temperature was calculated based on the experimental result.

$$\text{MAPE} = \frac{100}{n}\sum_{i=1}^{n}\left|\frac{T_i - \hat{T}_i}{T_i}\right| \tag{14}$$

where the T_i, $\hat{T}_i$, and n are the experimental record, the simulated result, and a number of variation, respectively. As shown in Table 5, the coefficient of friction equal to 0.9 had a minimum error for simulated temperature. Therefore, for the further simulation, the coefficient of friction of 0.9 was considered.

Figure 7a shows the temperature history measured by thermocouples of two points on each side of the center line (4 mm and 8 mm from the center line). The peak temperature was attained almost at the same time for all the thermocouples. Figure 7b compares the experimental and simulated peak temperature profile away from the stirring zone center line both in advancing and retreating sides 5 s after the beginning of stirring phase. The simulated results match well with the recorded one on each side of the center line. The results show that temperature distribution is asymmetrical with respect to the center line and it is higher in the advancing side compared to the retreating side. This agrees with the simulation work on friction stir welding [76]. The tool moves relatively faster in the advancing side with respect to work material compared to the retreating side. That contributes to a higher strain rate, thus, resulting in higher plastic deformation and frictional heat generation. The maximum temperature was recorded at advancing side which was 496 °C and was about 78% of the melting point of AA 5083, which is typically required in friction stir processes to achieve target microstructure and material properties of the processed area [1, 2].

The force signal in all three steps of the FSP process is compared with the experimentally measured force signal as shown in Fig. 8. For both of axial and transverse force, a good agreement was obtained between experimental and numerical results. With the friction coefficient equals to 0.9, the predicted axial force was 13% over-predicted, and transverse force was under-predicted by 32%.

Additionally, plastic strain plays a critical role in microstructure formation and grain size of the processed area. Contour plots of the equivalent plastic strain of the work material at the back side of the tool are compared with the experimental micrograph of the cross-section of the workpiece in Fig. 9. The equivalent plastic strain is highest at the center and decreases as moved away from the center. It is also higher near the surface decreases as moved deep into the workpiece. The stirred zone formed by tool rotation in the center line and therefore the higher strain can be seen at the center of the workpiece. The shape and area of nugget zone, TMAZ and

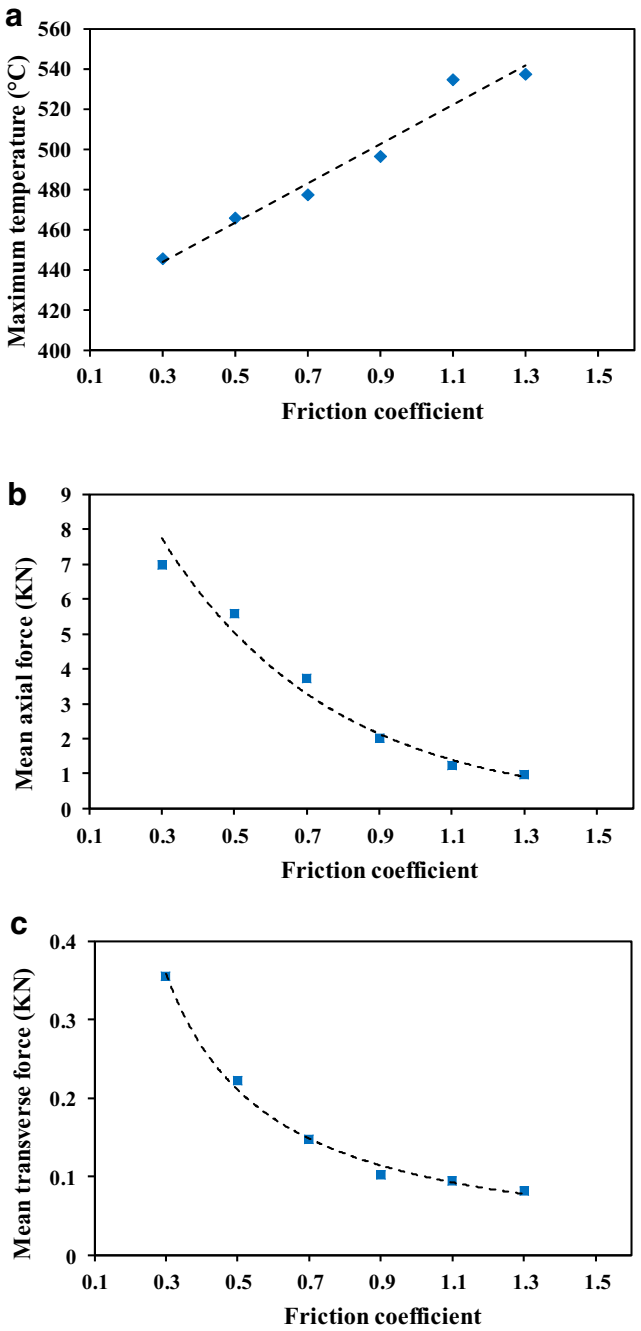

Fig. 6 Effect of the coefficient of friction on model outputs: **a** peak temperature, **b** average axial force during the stirring phase, and **c** average transverse force during stirring phase

Table 5 MAPE of temperature prediction using different coefficients of friction

Coefficient of friction	MAPE
0.3	36.1
0.5	21.1
0.7	12.5
0.9	9.7
1.1	18.4
1.3	27.2

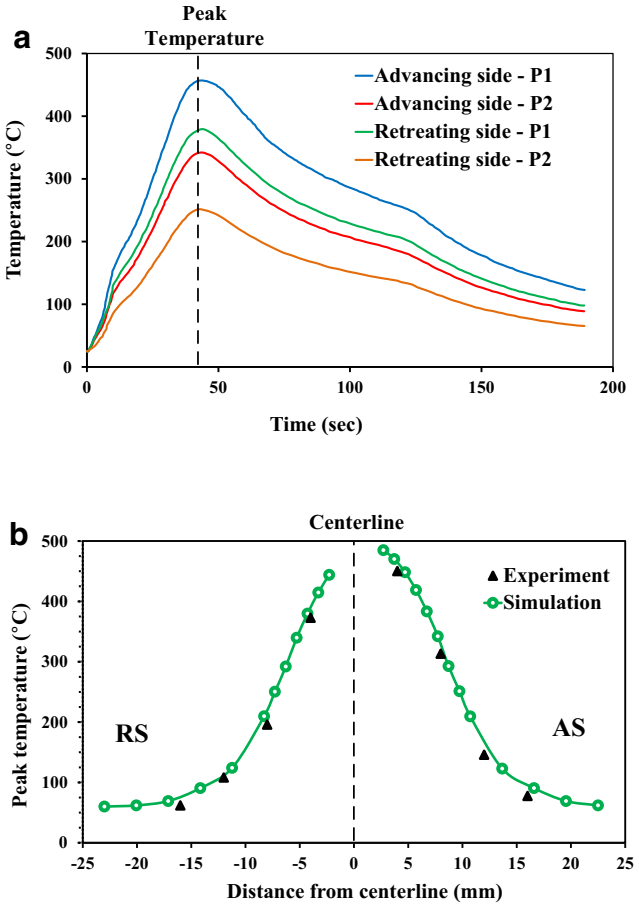

Fig. 7 Temperature measurement and predictions: **a** Temperature measurement using thermocouples; **b** comparison between experimental and simulated temperature distribution away from the workpiece center line

HAZ zone have a good agreement with the equivalent strain distribution.

Figure 10a shows high-magnification cross-sectional OM images transition zone between the processed zone and a base material which includes nugget, TMAZ, and HAZ regions. It can be observed that there is a significant difference between the microstructures of different regions. Fine equiaxed grains can be observed in the nugget area. The grains in nugget experience severe plastic deformation that leads to dynamic recrystallization to generate fine equiaxed grains. TMAZ is found in the close vicinity of the nugget. It is subjected to the thermal cycle and plastic deformation. Although the TMAZ underwent plastic deformation, recrystallization did not occur in this zone due to insufficient deformation strain. The HAZ is between the TMAZ and base material, a zone which only experiences a thermal cycle but does not undergo any plastic deformation. Hence, this region still retains the similar microstructure to the base material. The optical micrograph of Nugget zone with higher magnification is also presented in Fig. 10b showing a uniform distribution of fine-equiaxed grains.

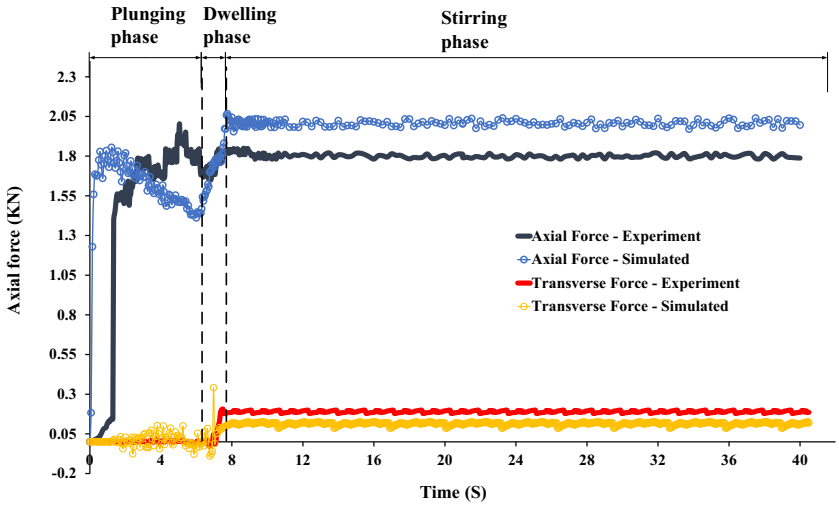

Fig. 8 Comparison between experiment and simulated axial and transverse force

4.2 Effect of tool-rotational speed

During the stirring phase of the FSP process, the temperature is generated due to frictional heat and plastic deformation. It is critical for the process to reach close to 0.8 T_m beneath the tool shoulder to keep the material in a malleable state and gain proper material stirring that defines the final properties of the material [1, 2]. Tool-rotational speed is the most essential process parameter to influence the generation of frictional heat and flow of the material. Four different rotational speeds were investigated in this section with the same plunging speed and traverse speed. Figure 11a shows the comparison of simulated and experimental maximum temperature at a location 4 mm away from the center line on the advancing side during the stirring phase for different rotational speeds. The peak temperature was increased with the increase of rotational speed because of the higher heat generation at the tool-workpiece interface at higher rotational speed. As the material gets more softened at higher speed, less force is required to deform the material. Figure 11b shows the comparison of simulated and experimental axial force at different tool-rotational speeds. The simulated peak temperature and axial force agree well with the experimentally measured values.

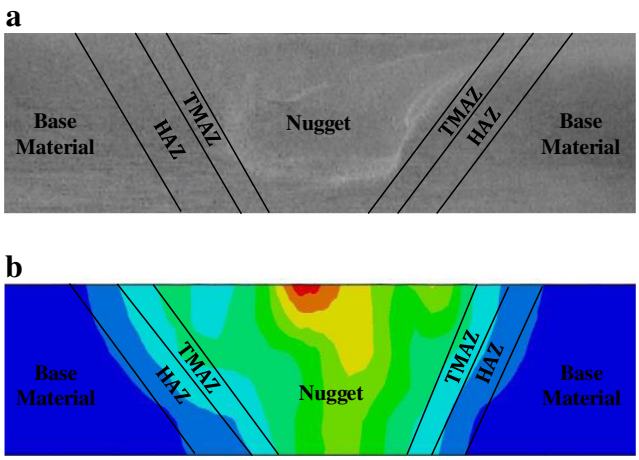

Fig. 9 Comparison of **a** etched stirred zone cross-section and **b** simulated equivalent plastic strain distribution

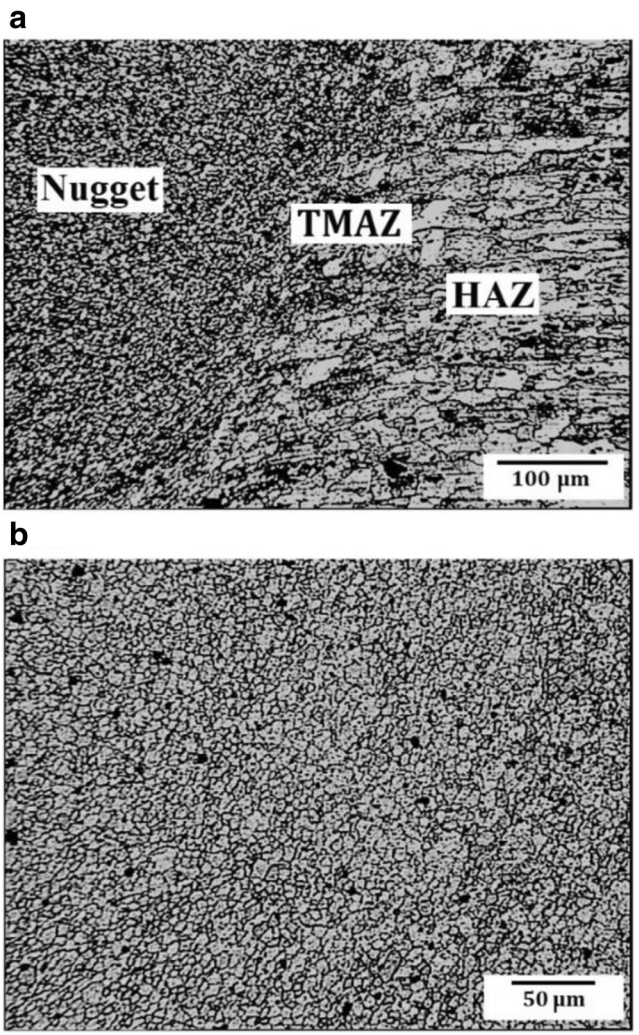

Fig. 10 Optical micrograph of **a** transition zone **b** nugget

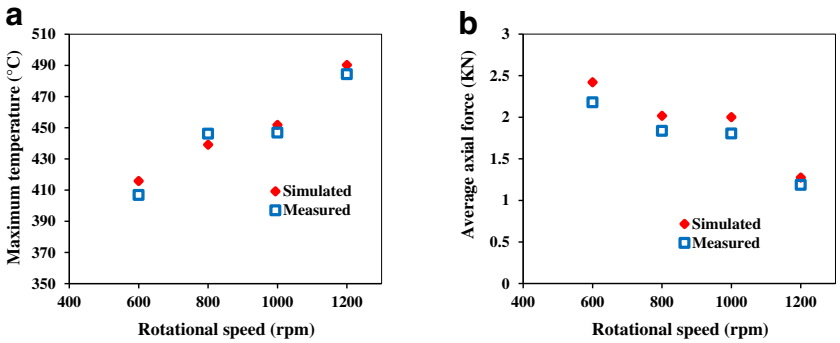

Fig. 11 Effect of tool-rotational speed on **a** maximum temperature at 4 mm from the center line and **b** average axial force during stirring phase

The contour plot of the effective strain rate distribution at the cross-section of the processing zone is illustrated in Fig. 12, which shows that the strain rate is on the order of 10^3 1/s. This value is consistent with the previous work by

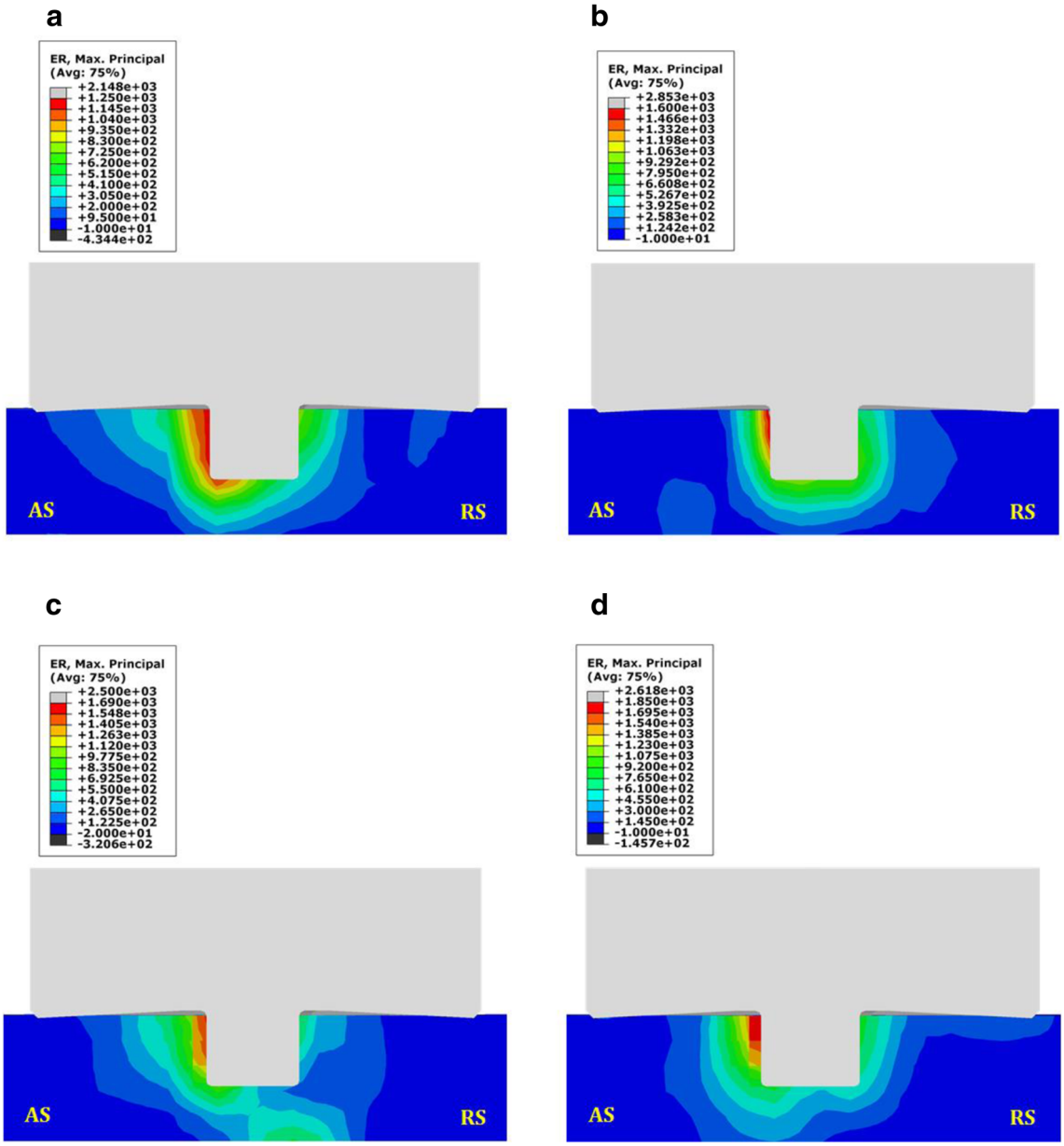

Fig. 12 Equivalent plastic strain rate distribution for rotational speed of **a** 600, **b** 800, **c** 1000, and **d** 1200 rpm

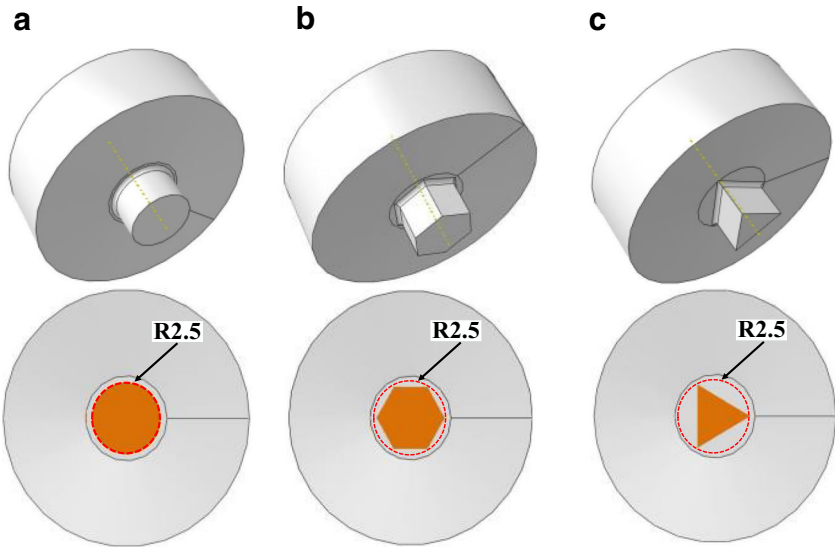

Fig. 13 Other pin profile geometry used in this study: **a** circular, **b** hexagonal, **c** triangular

Pan et al. [76] for friction stir welding. As the tool-rotational speed increases, the strain rate increases because higher rotational speed leads to higher tangential stirring velocity around the tool pin. As a result, material deformation rate increases leading to a higher strain rate. The strain rate around the tool increases by 48% as the rotational speed increases from 600 to 1200 rpm.

4.3 Effect of tool geometry

Friction stir tool geometry plays a vital role in the material stirring and needs to be optimized to achieve desirable surface properties [27]. Therefore, in addition to the above cuboid pin shape, the effect of three more different pin types was investigated for the same rotational speed of 1000 rpm and traverse speed of 50 mm/min. In all cases, the tool has a shoulder diameter of 18 mm, the constant tilt angle of 3°, and the pin is extruded vertically to the tool face with the shoulder concave angle of 3° (as shown in Fig. 13). All four pin profiles have the same sweep diameter of 5 mm.

The peak temperature is maximum for the circular tool pin geometry whereas it is minimum for the triangular tool pin geometry (Fig. 14a). The peak temperature of cuboid and hexagonal tool fall in between. The contact surface area of the tool pin plays the dominating role for this temperature difference. As it can be seen that the surface area of the triangular tool is the lowest and that of the circular tool is the highest, and that of the cuboid and hexagonal tool pin fall in between. As the tool pin surface area increases, the frictional contact area between tool and work material increases as well. This results in more frictional heat generation in case of circular tool compared to other three tools. Furthermore, higher frictional heat generation leads to higher thermal softening of deformed material around the pin area which helps to reduce the average axial force as shown in Fig. 14b.

4.4 Computational cost analysis

The computational cost of the developed model was compared with literature data of other existing models to show the improvement of the computational efficiency of the model. For the early FE packages, the simulation time for friction stir welding was more than a week to simulate a single second of processing time [77, 78]. However, with the recent progress

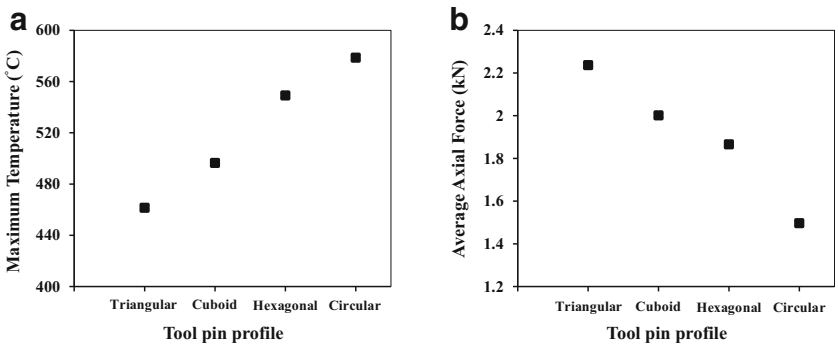

Fig. 14 Effect of pin profile on **a** peak temperature, and **b** average axial force during stirring phase

in the FE software and computational tools, the simulation runtime was much reduced for the friction stir process simulation. Using the ALE formulation, Assidi et al. [37] simulated the friction stir welding process in 12 days and 20 h for 10 s of actual processing time. Later, they used Eulerian formulation to simulate the same process in 6 days and 14 h for the same processing time, thus reducing the simulation time almost by half. In the current study, the Intel(R) Xeon(R) central processing unit with 14 cores at 2.6 GHz and 128 GB of RAM were used to simulate the FSP process using CEL formulation with mass scaling. Using this modeling technique, the total run time was around 3 days for simulating 41 s of actual processing time. It shows that the model developed in this study is significantly computation-efficient to simulate friction stir processing. The efficiency of this model is improved compared to concurrent CEL models for FSW processes due to the implementation of three strategies. Firstly, mass scaling technique has been implemented in this model. Navier's equation is scaled in terms of mass. It results in a small steady time increment of the explicit solver which decreases the simulation time. Secondly, in comparison to the other simulation frameworks such as Lagrangian and ALE, the CEL formulation does not require super fine mesh to tackle the mesh distortion or need any remeshing/remapping that increases the computational efficiency. Finally, the biased-meshing technique is applied to generate a fine mesh in the interaction region and coarse mesh in the sides which also contribute to the modeling efficiency.

5 Conclusions

A novel thermomechanical 3D FE model using CEL formulation was successfully developed for FSP to simulate process response. All the three steps of FSP, i.e., plunging, dwelling, and stirring, were simulated in ABAQUS/Explicit. Mass scaling technique was implemented to improve computational efficiency. The friction coefficient was determined to be 0.9 at the tool-workpiece interface by calibration using the measured temperature and force value. The simulated temperature profile in both advancing and retreating side agreed well with the experiments. The simulated force profile and contour plot of an equivalent plastic strain of the cross-section of the workpiece were also validated with experimentally recorded force signal and micrograph, respectively. The simulation demonstrated that process temperature, strain rate, and force profiles during friction stir processing were highly dependent on the tool-rotational speed. As the tool-rotational speed increased from 600 to 1200 rpm, temperature, and strain rate increased by 18%, and 48% respectively while the axial force decreased by 40%. Effect of different tool pin profile was also investigated in this work. Four different tool pin geometry, i.e., triangular, cuboid, hexagonal, and circular are studied. As the tool pin surface is increased, more frictional heat generated due to the higher frictional surface interaction between the tool and work material which led to the increase of peak temperature in the stirring zone and reduction average axial force.

Funding information The authors gratefully acknowledge the financial support provided for part of the study carried out at the University of Iowa by the National Science Foundation under Grant No. CMMI-1537512.

References

1. Węglowski MS (2018) Friction stir processing – state of the art. Arch Civ Mech Eng 18(1):114–129
2. Mishra RS, Ma ZY (2005) Friction stir welding and processing. Mater Sci Eng R 50(1–2):1–78
3. Ma ZY (2008) Friction stir processing technology: a review. Metall Mater Trans A 39(3):642–658
4. Jain R, Kumari K, Kesharwani RK, Kumar S, Pal SK, Singh SB, Panda SK, Samantaray AK (2015) Friction stir welding: scope and recent development. In: Davim JP (ed) Modern manufacturing engineering. materials forming, machining and tribology. Springer, Cham, pp 179–229.
5. Zimmer S, Langlois L, Laye J, Bigot R (2010) Experimental investigation of the influence of the FSW plunge processing parameters on the maximum generated force and torque. Int J Adv Manuf Technol 47(1–4):201–215
6. Khairuddin JT, Almanar IP, Abdullah J, Hussain Z (2012) Principles and thermo-mechanical model of friction stir welding. In: Kovacevic R (ed) Welding Processes, IntechOpen, pp 191-216
7. Meyghani B, Awang M, Emamian SS, Mohd Nor MK, Pedapati SR (2017) A comparison of different finite element methods in the thermal analysis of friction stir welding (FSW). Metals (Basel) 7(11):450
8. Fehrenbacher A, Duffie NA, Ferrier NJ, Pfefferkorn FE, Zinn MR (2014) Effects of tool-workpiece Interface temperature on weld quality and quality improvements through temperature control in friction stir welding. Int J Adv Manuf Technol 71(1–4):165–179
9. Cole EG, Fehrenbacher A, Duffie NA, Zinn MR, Pfefferkorn FE, Ferrier NJ (2014) Weld temperature effects during friction stir welding of dissimilar aluminum alloys 6061-T6 and 7075-T6. Int J Adv Manuf Technol 71(1–4):643–652
10. Leal RM, Loureiro A (2004) Defects formation in friction stir welding of aluminium alloys. Mater Sci Forum 455–456:299–302
11. Thomas, W. M., Nicholas, E. D., Needham, J. C., Murch, M. G., Temple-Smith, P., and Dawes, C. J., 1995, "Friction welding"
12. Givi MKB, Asadi P (2014) Advances in friction stir welding and processing. Woodhead Publishing Ltd., Amsterdam
13. Yazdipour A, Shafiei MA, Dehghani K (2009) Modeling the microstructural evolution and effect of cooling rate on the nanograins formed during the friction stir processing of Al5083. Mater Sci Eng A 527(1–2):192–197
14. Sharma SR, Ma ZY, Mishra RS (2004) Effect of friction stir processing on fatigue behavior of A356 alloy. Scr Mater 51(3):237–241
15. Ma ZY, Sharma SR, Mishra RS (2006) Microstructural modification of as-cast Al-Si-Mg alloy by friction stir processing. Metall Mater Trans A Phys Metall Mater Sci 37(11):3323–3336

16. Selvam K, Ayyagari A, Grewal HS, Mukherjee S, Arora HS (2017) Enhancing the erosion-corrosion resistance of steel through friction stir processing. Wear 386–387(June):129–138
17. Liu Q, Ma QX, Chen GQ, Cao X, Zhang S, Pan J, Zhang G, Shi Q (2018) Enhanced corrosion resistance of AZ91 magnesium alloy through refinement and homogenization of surface microstructure by friction stir processing. Corros Sci 138:284–296
18. Karthikeyan L, Senthilkumar VS, Padmanabhan KA (2010) On the role of process variables in the friction stir processing of cast aluminum A319 alloy. Mater Des 31(2):761–771
19. Jata KV, Semiatin SL (2000) Continuous dynamic recrystallization during friction stir welding of high strength aluminum alloys. Scr Mater 43(8):743–749
20. McNelley TR, Swaminathan S, Su JQ (2008) Recrystallization mechanisms during friction stir welding/processing of aluminum alloys. Scr Mater 58(5):349–354
21. Murr L, Liu G, McClure J (1997) Dynamic recrystallization in friction-stir welding of aluminium alloy 1100. J Mater Sci Lett 6(22):1801–1803
22. Liu G, Murr LE, Niou CS, McClure JC, Vega FR (1997) Microstructural aspects of the friction-stir welding of 6061-T6 aluminum. Scr Mater 37(3):355–361
23. Mironov S, Onuma T, Sato YS, Kokawa H (2015) Microstructure evolution during friction-stir welding of AZ31 magnesium alloy. Acta Mater 100(18):301–312
24. Saeid T, Abdollah-zadeh A, Shibayanagi T, Ikeuchi K, Assadi H (2010) On the formation of grain structure during friction stir welding of duplex stainless steel. Mater Sci Eng A 527(24–25): 6484–6488
25. Rasouli S, Behnagh RA, Dadvand A, Saleki-Haselghoubi N (2016) Improvement in corrosion resistance of 5083 aluminum alloy via friction stir processing. Proc Inst Mech Eng Part L J Mater Des Appl 230(1):142–150
26. Sharifzadeh M, Ansari MA, Narvan M, Behnagh RA, Araee A, Besharati Givi MK (2015) Evaluation of wear and corrosion resistance of pure Mg wire produced by friction stir extrusion. Trans Nonferrous Met Soc China (English Ed) 25(6):1847–1855
27. Miranda, R., Gandra, J., and Vilaça, P., 2013, "Surface modification by friction based processes," Modern Surface Eng Treatments pp. 1–20
28. Gunter C, Miles MP, Liu FC, Nelson TW (2017) Solid state crack repair by friction stir processing in 304L stainless steel. J Mater Sci Technol 34(1):140–147
29. Luo XC, Zhang DT, Zhang WW, Qiua C, Chen DL (2018) Tensile properties of AZ61 magnesium alloy produced by multi-pass friction stir processing: effect of sample orientation. Mater Sci Eng A 725(April):398–405
30. Zhang W, Ding H, Cai M, Yang W, Li J (2018) Ultra-grain refinement and enhanced low-temperature superplasticity in a friction stir-processed Ti-6Al-4V alloy. Mater Sci Eng A 727(March):90–96
31. Shokri V, Sadeghi A, Sadeghi MH (2018) Thermomechanical modeling of friction stir welding in a Cu-DSS dissimilar joint. J Manuf Process 31:46–55
32. Iordache M, Badulescu C, Iacomi D, Nitu E, Ciuca C (2016) Numerical simulation of the friction stir welding process using coupled Eulerian Lagrangian method. IOP Conf Ser Mater Sci Eng 145(2):022017
33. Chen K, Liu X, Ni J (2017) Thermal-mechanical modeling on friction stir spot welding of dissimilar materials based on coupled Eulerian-Lagrangian approach. Int J Adv Manuf Technol 91(5–8): 1697–1707
34. Al-Badour F, Merah N, Shuaib A, Bazoune A (2013) Coupled Eulerian Lagrangian finite element modeling of friction stir welding processes. J Mater Process Technol 213(8):1433–1439
35. Al-Badour F, Merah N, Shuaib A, Bazoune A (2014) Thermo-mechanical finite element model of friction stir welding of dissimilar alloys. Int J Adv Manuf Technol 72(5–8):607–617
36. Ajri A, Shin YC (2017) Investigation on the effects of process parameters on defect formation in friction stir welded samples via predictive numerical modeling and experiments. J Manuf Sci Eng 139(11):111009
37. Assidi M, Fourment L, Guerdoux S, Nelson T (2010) Friction model for friction stir welding process simulation: calibrations from welding experiments. Int J Mach Tools Manuf 50(2):143–155
38. Assidi M, Fourment L (2009) Accurate 3D friction stir welding simulation tool based on friction model calibration. Int J Mater Form 2(SUPPL. 1):327–330
39. Mandal S, Rice J, Elmustafa AA (2008) Experimental and numerical investigation of the plunge stage in friction stir welding. J Mater Process Technol 203(1–3):411–419
40. Guerdoux S (2004) Numerical simulation of the friction stir welding process using both Lagrangian and arbitrary Lagrangian Eulerian formulations. AIP Conf Proc 712(2004):1259–1264
41. Bussetta P, Dialami N, Boman R, Chiumenti M, Agelet De Saracibar C, Cervera M, Ponthot JP (2014) Comparison of a fluid and a solid approach for the numerical simulation of friction stir welding with a non-cylindrical pin. Steel Res Int 85(6):968–979
42. de Saracibar CA, Chiumenti M, Cervera M, Dialami N, Seret A (2014) Computational modeling and sub-grid scale stabilization of incompressibility and convection in the numerical simulation of friction stir welding processes. Arch Comput Methods Eng 21(1): 3–37
43. Chiumenti M, Cervera M, Agelet de Saracibar C, Dialami N (2013) Numerical modeling of friction stir welding process. Comput Methods Appl Mech Eng 254:353–369
44. Dialami N, Chiumenti M, Cervera M, Agelet De Saracibar C, Ponthot JP (2015) Material flow visualization in friction stir welding via particle tracing. Int J Mater Form 8:167–181
45. Chauhan P, Jain R, Pal SK, Singh SB (2018) Modeling of defects in friction stir welding using coupled Eulerian and Lagrangian method. J Manuf Process 34(November 2017):158–166
46. Chu Q, Yang XW, Li WY, Vairis A, Wang WB (2018) Numerical analysis of material flow in the probeless friction stir spot welding based on coupled Eulerian-Lagrangian approach. J Manuf Process 36(July):181–187
47. Hossfeld M 2016, "A fully coupled thermomechanical 3D model for all phases of friction stir welding," 11th Int. Symp. Frict. Stir Welding, Cambridge
48. Cao JY, Wang M, Kong L, Yin YH, Guo LJ (2017) Numerical modeling and experimental investigation of material flow in friction spot welding of Al 6061-T6. Int J Adv Manuf Technol 89(5–8): 2129–2139
49. Grujicic M, Arakere G, Pandurangan B, Ochterbeck JM, Yen CF, Cheeseman BA, Reynolds AP, Sutton MA (2012) Computational analysis of material flow during friction stir welding of AA5059 aluminum alloys. J Mater Eng Perform 21(9):1824–1840
50. Ding H, Shen N, Shin YC (2012) Predictive modeling of grain refinement during multi-pass cold rolling. J Mater Process Technol 212(5):1003–1013
51. Ding H, Shin YC (2012) A metallo-thermomechanically coupled analysis of orthogonal cutting of AISI 1045 steel. J Manuf Sci Eng 134(5):051014
52. Ding H, Shin YC (2014) Dislocation density-based grain refinement modeling of orthogonal cutting of titanium. Trans ASME, J Manuf Sci Eng 136(4):041003
53. Behnagh RA, Shen N, Ansari MA, Narvan M, Besharati Givi MK, Ding H (2015) Experimental analysis and microstructure modeling of friction stir extrusion of magnesium chips. J Manuf Sci Eng 138(4):041008

54. Ducobu F, Arrazola PJ, Rivière-Lorphèvre E, Zarate GO, De Madariaga A, Filippi E (2017) The CEL method as an alternative to the current modelling approaches for Ti6Al4V orthogonal cutting simulation. Procedia CIRP 58:245–250
55. Tutunchilar S, Haghpanahi M, Besharati Givi MK, Asadi P, Bahemmat P (2012) Simulation of material flow in friction stir processing of a cast Al-Si alloy. Mater Des 40:415–426
56. Zhang Z, Zhang HW (2009) Numerical studies on controlling of process parameters in friction stir welding. J Mater Process Technol 209(1):241–270
57. Schmidt H, Hattel J, Wert J (2004) An analytical model for the heat generation in friction stir welding. Model Simul Mater Sci Eng 12(1):143–157
58. Benson DJ, Okazawa S (2004) Contact in a multi-material eulerian finite element formulation. Comput Methods Appl Mech Eng 193(39–41 SPEC. ISS):4277–4298
59. Benson DJ (1997) A mixture theory for contact in multi-material Eulerian formulations. Comput Methods Appl Mech Eng 140(1–2): 59–86
60. Spencer AJM (2004), Continuum mechanics, Courier Corporation
61. Jain R, Pal SK, Singh SB (2016) A study on the variation of forces and temperature in a friction stir welding process: a finite element approach. J Manuf Process 23:278–286
62. Lee SL, Ou CR (2001) Gap formation and interfacial heat transfer between thermoelastic bodies in imperfect contact. J Heat Transf 123(2):205
63. Holman J (1997) Heat transfer. McGraw-Hill, New York
64. Li W, Zhang Z, Li J, Chao YJ (2012) Numerical analysis of joint temperature evolution during friction stir welding based on sticking contact. J Mater Eng Perform 21(9):1849–1856
65. Li H, MacKenzie D, Hamilton R (2010) Parametric finite-element studies on the effect of tool shape in friction stir welding. Proc Inst Mech Eng Part B J Eng Manuf 224(8):1161–1173
66. Zhu Z, Wang M, Zhang H, Zhang X, Yu T, Wu Z (2017) A finite element model to simulate defect formation during friction stir welding. Metals (Basel) 7(7):256
67. Schmidt H, Hattel J (2005) A local model for the thermomechanical conditions in friction stir welding. Model Simul Mater Sci Eng 13(1):77–93
68. Hammelmüller F, and Zehetner C (2015), "Increasing numerical efficiency in coupled Eulerian-Lagrangian metal forming simulations," Proceedings of the XIII International Conference on Computational Plasticity. Fundamentals and Applications, Barcelona, Spain, pp. 727–733
69. Nicholson DW (2008) Finite element analysis: Thermomechanics of solids, CRC Press
70. Johnson GR, and Cook WH (1983) "A constitutive model and data for metals subjected to large strains, high strain rates and high temperatures," Proceedings of the 7th International Symposium on Ballistics, the Netherlands
71. Kim D, Badarinarayan H, Kim JH, Kim C, Okamoto K, Wagoner RH, Chung K (2010) Numerical simulation of friction stir butt welding process for AA5083-H18 sheets. Eur J Mech A/Solids 29(2):204–215
72. Aval HJ, Serajzadeh S, Kokabi AH (2011) Evolution of microstructures and mechanical properties in similar and dissimilar friction stir welding of AA5086 and AA6061. Mater Sci Eng A 528(28):8071–8083
73. Van Der Steen R (2007) Tyre / road friction modeling literature survey
74. Lorrain O, Serri J, Favier V, Zahrouni H, El Hadrouz M (2009) A contribution to a critical review of friction stir welding numerical simulation. J Mech Mater Struct 4(2):351–369
75. Li W, Shi S, Wang F, Zhang Z, Ma T, Li J (2012) Numerical simulation of friction welding processes based on ABAQUS environment. J Eng Sci Technol Rev 5(3):10–19
76. Pan W, Li D, Tartakovsky AM, Ahzi S, Khraisheh M, Khaleel M (2013) A new smoothed particle hydrodynamics non-Newtonian model for friction stir welding: process modeling and simulation of microstructure evolution in a magnesium alloy. Int J Plast 48: 189–204
77. Awang M (2007) "Simulation of friction stir spot welding (FSSW) process : study of friction phenomena," West Virginia University
78. Lasley MJ (2005) "A finite element simulation of temperature and material flow in friction stir welding," Brigham Young University - Provo